When do Anisotropic Magnetic Susceptibilities Lead to Large NMR Shifts? Exploring Particle Shape Effects in the Battery Electrode Material $LiFePO_4$

Roberta Pigliapochi,[†] Liam O'Brien,[‡] Andrew J. Pell,[†,§] Michael W. Gaultois,[†,‖] Yuri Janssen,[¶,⊥] Peter Khalifah,[¶] and Clare P. Grey[*,†]

[†]*Department of Chemistry, University of Cambridge, CB2 1EW Cambridge, UK*

[‡]*Department of Physics, University of Liverpool, L69 7ZE Liverpool, UK*

[¶]*Department of Chemistry, Stony Brook University, NY 11794 Stony Brook, United States*

[§]*Current Address: Department of Materials and Environmental Chemistry, Stockholm University, SE–106 91 Stockholm, Sweden*

[‖]*Current Address: Leverhulme Research Centre for Functional Materials Design, The Materials Innovation Factory, Department of Chemistry, University of Liverpool, Liverpool L7 3NY, UK*

[⊥]*Current Address: Department of Physics, Farmingdale State College, NY 11735 Farmingdale, United States*

E-mail: cpg27@cam.ac.uk

Abstract

Materials used as electrodes in energy storage devices have been extensively studied with solid-state NMR spectroscopy. Due to the almost ubiquitous presence of transition

metals, these systems are also often magnetic. While it is well known that the presence of anisotropic bulk magnetic susceptibility (ABMS) leads to broadening of resonances under MAS, we show that for mono-disperse and non-spherical particle morphologies, the ABMS can also lead to considerable shifts, which vary substantially as a function of particle shape. This, on one hand, complicates the interpretation of the NMR spectrum and the ability to compare the measured shift of different samples of the same system. On the other hand the ABMS shift provides a mechanism with which to derive the particle shape from the NMR spectrum. In this work, we present a methodology to model the ABMS shift, and relate it to the shape of the studied particles. The approach is tested on the ^{7}Li NMR spectra of single crystals and powders of $LiFePO_4$. The results show that the ABMS shift can be a major contribution to the total NMR shift in systems with large magnetic anisotropies and small hyperfine shifts, ^{7}Li shifts for typical $LiFePO_4$ morphologies varying by as much as 100 ppm. The results are generalised to demonstrate that the approach can be used as a means with which to probe the aspect ratio of particles. The work has implications for the analysis of NMR spectra of all materials with anisotropic magnetic susceptibilities, including diamagnetic materials such as graphite.

Introduction

Solid-state nuclear magnetic resonance (NMR) spectroscopy represents a powerful technique to probe the short-range structural ordering and electronic properties of solids. When applied to paramagnetic systems, the NMR response is sensitive to the number, connectivity and oxidation state of the paramagnetic ions surrounding the NMR observed nucleus, as well as the bulk magnetic properties of the system.[1–9] Materials used as electrodes in energy storage devices represent a wide class of paramagnetic solids that are often studied with solid-state NMR. In this regard, NMR has proven to be extremely effective in investigating the local structure and (dis)order as a function of synthesis and electrochemical conditions.[10,11] The

morphology of the particles constituting the electrodes is also a very important aspect to control, as many of the properties of the material in the electrochemical device depend on particle shape and size.[12–14] It has been shown that solid-state NMR can be used to determine the sizes of domains in polymer systems in the nanometre–micrometre range, using a variety of approaches. Previous studies measured spin diffusion,[15–17] or first impregnated the sample with a paramagnetic species, and measured spin-diffusion-relayed paramagnetic relaxation enhancement (PRE)[18] or dynamic nuclear polarization (DNP) enhancement[19] within the domain. However, whilst these methods have proved efficacious at measuring domain *sizes*, it has proved particularly difficult to determine their *shapes*.[20] It is precisely this important point that we address in this paper, demonstrating the approach for a paramagnetic electrode material.

In the NMR spectrum of a paramagnetic solid, several different short and long-range interactions may contribute to the shift and shift anisotropy for a given nucleus, and are often difficult to disentangle.[1,21–24] In the presence of spin-orbit coupling, hyperfine interactions between the observed nuclear spin and the unpaired spin density of the paramagnetic centres produce contributions to both the isotropic shift (Fermi contact and pseudo-contact shifts)[10,22,23] and shift anisotropy (anisotropic hyperfine interaction, relativistic dipolar and relativistic contact contributions).[1,25,26] In addition to these local interactions, the macroscopic magnetic properties of the system may also affect the NMR spectrum.[1,8,9,27–31] When any finite-sized para- or dia-magnetic sample is placed in a magnetic field, the induced moment arising from the bulk magnetic susceptibility (BMS) of the material generates a demagnetising field. This field either adds to or opposes the static external field[32] and, depending on the anisotropy of both the BMS and of the sample shape (be it a single crystal or a powder), can contribute to both the shift and shift anisotropy of the NMR spectrum,[8,28,29] and the spinning sideband intensities under magic angle spinning (MAS).[33] Ultimately, the Fermi contact, pseudo-contact and BMS shifts, as well as the dipolar and the BMS shift anisotropies, are additive, and untangling these contributions to rationalize the NMR spec-

trum of a paramagnetic material requires the ability to quantify them separately.

Early pioneering work by VanderHart[30] and Alla and Lippmaa[31] showed that BMS effects can constitute an additional source of inhomogeneous line broadening in the NMR spectra. Schwerk *et al.*[27] and Kubo *et al.*[28] presented a theoretical derivation of the isotropic BMS (IBMS) and anisotropic BMS (ABMS) effects on the NMR spectrum of homogeneous paramagnetic powders. Dickinson *et al.*[34] extended the model based on classical electrostatics to calculate the demagnetizing fields of bulk samples, and the corresponding effects on the NMR spectrum of inhomogeneous materials. However, the explicit dependence on the single crystal geometry or, in the case of powders, crystallite geometry, distribution, and even container shape,[8] means that the model to calculate the BMS effects must typically be derived on a sample-to-sample basis. In previous in situ NMR studies of pouch-cell type batteries containing the paramagnetic material lithium manganese spinel ($LiMn_2O_4$), some of the present authors showed that significant NMR shifts were induced that depended on the orientation of the battery electrodes with respect to the magnetic field.[8,9] This phenomenon was modelled by calculating the dipolar fields that originated from the isotropic magnetic susceptibilities of single crystals with the same aspect ratios as the pouch-cell batteries. The studies showed that, by appropriately orientating the single crystal (and battery) to the magnetic field, the BMS shift could be removed. Here we show for the first time, that ABMS effects can lead, in addition to the previously discussed ABMS broadening of resonances, significant isotropic shifts that cannot be removed by MAS. Of note, we demonstrate for the electrode material $LiFePO_4$ that the shift depends on particle shape, an observation that can be exploited to determine aspect ratios of particles.

$LiFePO_4$ is an example of a paramagnetic system which has been extensively studied over the last few decades for its application as a cathode material in rechargeable Li–ion batteries.[35] The unit cell of the olivine-type $LiFePO_4$ structure (*Pnma* space group) contains one unique Li crystallographic site in octahedral coordination, connected *via* the oxygens to six octahedral Fe^{2+} ions (in high-spin d^6 oxidation state, hence having four unpaired d

electrons).[36,37] When studied with solid-state NMR, the ^{7}Li spectrum of $LiFePO_4$ does indeed show a single resonance, broadened by paramagnetic effects, that is characteristic of the one Li crystallographic site in the structure. However, despite the purity and the crystallinity of the studied materials, the value of the ^{7}Li NMR shift reported in the literature by different groups varies noticeably ranging from 0 ppm to close to -60 ppm.[38–43] The reason for this widespread discrepancy is a source of debate, and it represented the original motivation for the studies that we report here.

This work analyzes the previously untreated combination of anisotropic crystal shape and ABMS and shows that this can generate substantial isotropic MAS shifts. Specifically, we investigate the bulk magnetic susceptibility effects on the ^{7}Li NMR shift and shift anisotropy in $LiFePO_4$. A series of $LiFePO_4$ single crystals of different morphologies is studied with static and MAS ^{7}Li NMR. The morphologies of the samples are also implemented in a mathematical model, which is used to calculate the ABMS contribution to the ^{7}Li NMR parameters for each crystal. The substantial differences in the measured ^{7}Li NMR spectra between the studied $LiFePO_4$ samples are explained based on the shape dependence of the ABMS effects. Motivated by the agreement between the experimental and calculated ^{7}Li NMR spectra for the single crystals, the analysis is extended to the ^{7}Li NMR shift in $LiFePO_4$ powders with different crystallite morphologies. A range of $LiFePO_4$ particle shapes previously reported in the literature are simulated, and the BMS contribution to the ^{7}Li NMR shift is calculated. The results identify a trend of ^{7}Li NMR shift variation as a function of particle shape in both single crystals and powders, providing an explanation for the wide variability in isotropic shift observed throughout the literature for $LiFePO_4$. Of note, this work shows that for powdered samples with uniform particle shapes, and anisotropic magnetic susceptibilites, significant contributions to the isotropic shifts, in addition to broadening, can result from ABMS effects.

Theory

When an external magnetic field, H_0, is applied to a paramagnetic crystal, a net magnetic moment μ_{ind} parallel to H_0 is induced. In a macroscopic continuum approximation, this moment can be described by a magnetisation per unit volume, M, which is proportional to the external field,[44]

$$M = \frac{\mu_{\text{ind}}}{V} = \chi_{\text{V}} H_0, \tag{1}$$

where V is the total crystal volume, and χ_{V} is the volume magnetic susceptibility. If the electron orbital angular momentum, and spin-orbit coupling effects, are non-negligible, the volume magnetic susceptibility becomes a tensor, $\boldsymbol{\chi}_{\text{V}}$, with a spatially anisotropic part, and the total magnetic moment $\boldsymbol{\mu}$ and magnetization $\boldsymbol{M}$ vectors are no longer necessarily parallel to the external field. In this work we measure the molar magnetic susceptibility tensor $\boldsymbol{\chi}$, which is related to the volume susceptibility tensor via $\boldsymbol{\chi} = V_{\text{M}} \boldsymbol{\chi}_{\text{V}}$, where V_{M} is the molar volume of the material.

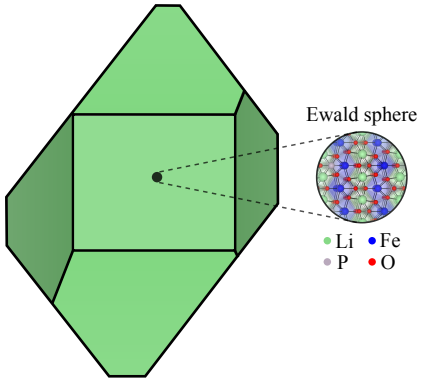

Figure 1: Schematic representation of the model of a paramagnetic $LiFePO_4$ crystal of arbitrary shape. The Ewald sphere is shown in the inset on the right-hand side, with a radius much smaller than the dimensions of the crystal, but sufficiently large so that the sum of the local interactions contributing to $\boldsymbol{\delta}^s$ converges. The remainder of the crystal is treated as an uniformly magnetized continuum within which the bulk magnetic susceptibility effects generate the $\boldsymbol{\delta}^{\text{BMS}}$ contribution to the total shift tensor of the NMR-observed nucleus I (in this example, $I = {}^7\text{Li}$.

We now examine how the magnetic susceptibility of the bulk material affects the NMR

spectrum of a paramagnetic sample. In this work, we use a similar approach to that of the Kubo model,[28] which is schematically represented in Figure 1. The model assumes that the NMR observed nucleus I is at the center of a local region, referred to as the Ewald sphere, which has dimensions much smaller than those of the crystal. Within this region, I experiences a local paramagnetic shift tensor, $\boldsymbol{\delta}^s$, resulting from the sum of the orbital shielding interaction and the paramagnetic shift tensor due to the hyperfine interactions with the nearby paramagnetic metal ions. The radius of the Ewald sphere is defined to be large enough so that the individual contributions of $\boldsymbol{\delta}^s$ converge. The remainder of the crystal is then assumed to be a uniformly magnetised continuum, from which the bulk magnetic susceptibility (BMS) effects contribute a BMS shift tensor, $\boldsymbol{\delta}^{\mathrm{BMS}}$. The total shift, $\boldsymbol{\delta}^{\mathrm{TOT}}$, at the observed nucleus, I, is hence given by the sum of these contributions:

$$\boldsymbol{\delta}^{\mathrm{TOT}} \;=\; \boldsymbol{\delta}^{s} \;+\; \boldsymbol{\delta}^{\mathrm{BMS}}. \tag{2}$$

The contributions of $\boldsymbol{\delta}^s$ to the NMR spectrum of a crystal(lite) can be determined experimentally. If the particles in a powder are isotropic (i.e. spherical or cubic in shape), so as to approximate the Ewald sphere described earlier, then the isotropic shift, measured under conditions of MAS, provides a good estimate of δ^{iso}. This approach will be followed in this work. The shift anisotropy measured for this powdered sample will still be affected by additional BMS broadening due to the local fields caused by nearby particles,[33] but experimental stratagems such as dilution of the particles in a diamagnetic medium and susceptibility matching help to separate the local and long range effects.

First principles calculations of the hyperfine and spin-orbit interactions defining $\boldsymbol{\delta}^s$ have been successfully applied to various paramagnetic systems, from molecules containing a single paramagnetic ion to solids with paramagnetic centres prevalent throughout the lattice,[5,6,45–48] and represent an independent method for estimating the local hyperfine tensor, $\boldsymbol{\delta}^s$. We note however that solid-state DFT approaches still do not accurately treat all of the

interactions, such as the zero field splitting, for which alternative computational approaches have been proposed, e.g. the incremental cluster model applied to molecular calculations.[49] We thus adopt a pragmatic approach, taking the isotropic shift from the MAS spectrum of the powder, but for completeness include a calculation using the DFT-derived full tensor in the supplemental information.

To determine $\boldsymbol{\delta}^{\mathrm{BMS}}$, one must consider the uniformly magnetised continuum, external to the Ewald sphere. The demagnetising field, $\boldsymbol{H}_D$, which is generated due to the discontinuity of $\boldsymbol{M}$ at the sample edges,[32,50] takes the form:

$$\boldsymbol{H}_D \;=\; -\,\boldsymbol{N}\cdot\boldsymbol{M} = -\boldsymbol{N}\cdot\boldsymbol{\chi_V}\cdot\boldsymbol{H}_0, \tag{3}$$

where $\boldsymbol{N}$ is the demagnetising tensor, with the rank-two part of $\boldsymbol{N}$ related to the deviation of the shape of the crystal from spherical symmetry. In general, $\boldsymbol{N}$, and so $\boldsymbol{H_D}$, is position dependent. However, in relatively simple crystal shapes (e.g. ellipsoids), $\boldsymbol{H_D} \parallel \boldsymbol{M}$ and $\boldsymbol{N}$ is uniform within the crystal. The trace $Tr(\boldsymbol{N})$ equals 1 at any position inside the volume of the crystal, and 0 at any point outside the crystal. Three examples of demagnetising tensors are presented in Figure S1 of the S.I. for crystals of different shapes. We note that, by definition, in any direction i where a given crystal dimension extends to inifinity, $N_{ii} = 0$.

In analogy with the nuclear Zeeman interaction, the demagnetising field essentially induces an additional shift at the nuclear spin, and the form of this $\boldsymbol{\delta}^{\mathrm{BMS}}$ inside the crystallite can be derived as,[1]

$$\boldsymbol{\delta}^{\mathrm{BMS}}(\boldsymbol{r}) \;=\; -\boldsymbol{\chi}_V\cdot\left(\boldsymbol{N}(\boldsymbol{r})^T \;-\; \frac{1}{3}\mathbf{1}\right) \tag{4}$$

where $\mathbf{1}$ is the identity matrix, and $\boldsymbol{r}$ is the position vector, the origin of which is the center of mass of the crystallite. This form of the BMS shift tensor indicates that, for a spherical crystal which has an isotropic demagnetizing tensor given by $\boldsymbol{N} = \mathbf{1}/3$, $\boldsymbol{\delta}^{\mathrm{BMS}}$ is zero. In this case the total shift tensor is simply the local contribution $\boldsymbol{\delta}^s$. Conversely, a shift in static spectra will be observed when the component of $\boldsymbol{\chi}_V\cdot\boldsymbol{N}(\boldsymbol{r})^T\cdot\boldsymbol{H_0} \neq 1/3$, i.e. for non-spherical

shape, as first described by Dickinson.[51] Following the work of Garroway[52] this IBMS shift is known to be removed under MAS, leaving only effects arising due to ABMS. VanderHart[30] and Alla[31] demonstrated that the ABMS generates significant broadening even under MAS, although any isotropic shift was reasoned to average to zero in this case, particularly for ellipsoids of revolution. However, inspection of the isotropic BMS shift $\delta_{\text{calc.}}^{\text{BMS}}$, calculated as:

$$\delta_{\text{calc.}}^{\text{BMS}} = -\frac{1}{3} Tr \left[\boldsymbol{\chi}_V \cdot \left(\boldsymbol{N}(\boldsymbol{r})^T \; - \; \frac{1}{3}\mathbf{1} \right) \right], \tag{5}$$

shows that appreciable $\delta_{\text{calc.}}^{\text{BMS}}$ can be observed in samples where the magnitude of $\boldsymbol{\chi}_V$ is large, and both $\boldsymbol{\chi}_V$ and $\boldsymbol{N}$ are anisotropic, i.e., in crystals that are far from spherical in shape (but still including ellipsoids). It is worth noting that, since we make no approximations of the form of $\boldsymbol{N}$ in equations 4 and 5, we implicitly include the conventional IBMS and ABMS terms (i.e. static shifts, and anisotropic line broadening) when calculating any effects of crystal shape. Although these terms are included, we are reminded that the conventional IBMS and ABMS terms ultimately do not contribute to $\delta_{\text{calc.}}^{\text{BMS}}$,[27,28] and we stress that is the previously untreated combination of anisotropic crystal shape and ABMS that generates isotropic MAS shifts.

In powder samples, additional terms arising from inter-crystallite dipole interactions and the finite container shape also generate BMS effects. Due to both the random orientation of the crystallites within the powder, and on averaging over the different relative positions of interacting crystallites, the central limit theorem determines there to be no net isotropic shift due to inter-crystallite dipolar coupling in powders. (This does not, however, preclude additional line broadening). Furthermore, the random orientation of the crystallites in the powder results in an isotropic volume-averaged (i.e. over length-scales larger than a single crystallite) BMS for the powder. This in turn means any contribution from finite container shape to $\delta_{\text{calc.}}^{\text{BMS}}$ is zero under MAS, as predicted by VanderHart[30] and derived explictly by Kubo.[28] Consequently, for $\delta_{\text{calc.}}^{\text{BMS}}$ in powder samples, we once again need only to consider *intra*-crystallite BMS effects, and so the combined ABMS and anistropic crystallite shape,

to obtain any isotropic BMS shifts.

In general, to quantify the demagnetising field and to compute $\boldsymbol{\delta}^{\mathrm{BMS}}$, one needs to know $\boldsymbol{N}$ and $\boldsymbol{\chi}_V$. In simple geometries, where $\boldsymbol{N}$ is uniform throughout the crystal, these can be analytically determined from the dimensions of the sample. In more complex shapes, however, $\boldsymbol{H}_D$ must be calculated numerically[28] using the precise sample geometry, as is the approach taken here.

Experimental Methods

$LiFePO_4$ Crystal Growth, Basic Characterization, Single Crystal Diffraction

Single crystals of $LiFePO_4$ were prepared and characterized by Janssen *et al.*, as described in detail in Ref. 53. To briefly summarize, the crystals were prepared by flux growth techniques, using Li_3PO_4, LiCl, $FeCl_2$ as reagents, heated to 810 °C, held at this temperature for 2 h and then slowly cooled to 480°C, after which the furnace was allowed to cool naturally. The growth boules were then taken out of the crucibles, and the LiCl-$FeCl_2$ flux was dissolved with water or ethanol in an ultrasonic bath to reveal the crystals. Alignment of the single crystals was performed using X-ray diffraction data collected at room temperature.

The three $LiFePO_4$ single crystals used in this study, labelled Crystal $1-3$ hereafter, are shown in Figure 2a as schematics (with photographs in Figure 2b). The dimensions of each crystal along the three principal axes (a, b, c) are given in Table 1. Although the shapes are non-trivial, we can make an approximate comparison between the different morphologies. The relative dimensions of Crystal 1 and 2 along the principal axes are similar, with $a < b < c$. In contrast, being more plate-like, Crystal 3 has $c < a < b$. We will see that this transition from long to short axis in c across the sample set has a dramatic effect on $\boldsymbol{N}$, driving the changes in BMS shift and therefore in the observed δ^{iso}.

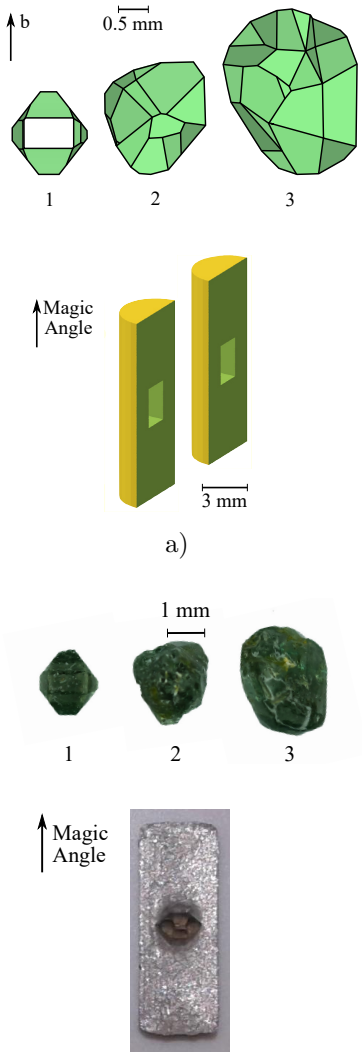

Figure 2: Images of the three $LiFePO_4$ crystals $1-3$, and the 3D-printed insert used to hold the crystals inside the 4 mm rotor for MAS experiments. In Fig. 2a) are shown schematic representations of the three $LiFePO_4$ single crystals, and the design of the 3D-printed insert for the 4 mm rotor. Fig. 2b) shows the corresponding photographs of the crystals, labelled Crystal $1-3$. The photograph of the 3D-printed insert shows Crystal 1 aligned with the a-axis parallel to the rotor axis (along the magic angle).

$LiFePO_4$ Powder XRD and TEM

The carbon-coated $LiFePO_4$ powder was synthesized by Strobridge *et al.*, *via* the solid-state method described in Ref. 54. The particle size of the $LiFePO_4$ powder was determined with powder X-ray diffraction (XRD) and transmission electron microscopy (TEM). Laboratory

X-ray diffraction (XRD) was performed with a PANalytical Empyrean diffractometer using Cu Kα radiation ($\lambda = 1.5406\,\text{Å}$), and Rietveld refinement was performed using the Topas Academic software package[55] using an initial model of $LiFePO_4$ from Nytén and Thomas.[56] A NIST Si standard was run prior to refinements to determine the instrument profile parameters, after which a size-strain analysis of $LiFePO_4$ was performed during the Rietveld refinement using a Voigt convolution as described and discussed by Balzar *et al.*[57,58] A total of 17 TEM images of the $LiFePO_4$ powder were obtained using a JEOL JEM-3010 Transmission Electron Microscope (300 kV). The particle size distribution was calculated by directly measuring the size of 30 different particles and averaging over their determined volumes.

Magnetic Measurements

Magnetization measurements were performed with a Quantum Design Material Property Measurement System (MPMS). Magnetic moments of zero field-cooled crystals were measured at temperatures from 2 K up to 301 K to obtain the temperature dependence of the magnetic susceptibility, $\chi(T) = dM/dH \approx M/H$. The unitless paramagnetic susceptibility of $LiFePO_4$ is approximately 3×10^{-3} at its largest value (along b axis), and so the screening correction of the applied field due to the demagnetising field is $< 0.3\%$. We note this is smaller than the rounding error on the values here measured, and so no correction is applied to the presented data. Each measurement was conducted by mounting the crystal in epoxy resin aligned along one of the *a*, *b* and *c* principal axes with respect to the external field. This allowed the characterization of the susceptibility tensor along the three principal components of each crystal.

Solid-state MAS ^{7}Li NMR

Solid-state ^{7}Li NMR spectra of the three $LiFePO_4$ crystals and of the $LiFePO_4$ powder sample were acquired on a Bruker 200 Avance III spectrometer using a 4 mm probe. For the MAS acquisitions, a spinning frequency of 12.5 kHz was used. The one-dimensional ^{7}Li

spectra were recorded using a double-adiabatic spin-echo sequence,[59] employing a pair of 50 μs tanh/tan short high-powered adiabatic pulses (SHAPs) of 5 MHz sweep width[60,61] and a 1.025 μs 90° excitation pulse. All pulses used a radiofrequency (RF) field strength of 244 kHz. For each spectrum, 8192 scans were acquired using a recycle delay of 30 ms. The pulse sequence used for the single-crystal MAS NMR was modified to include a *trigger* function, which allowed each scan to start at the same rotor rotation angle, in order to obtain the same side-band profile in each acquisition.[62] As a comparison, the same pulse sequence was also used without the inclusion of the *trigger* function. Without this option, the whole carousel is sampled by signal averaging, i.e. each pulse sequence starts at a random and potentially different rotor (hence crystal) rotation angle.[63] Over the entire set of scans, the sum of the collected spectra corresponding to an average of the rotation-specific side-band profiles, gives a fully in-phase side-band pattern.[62] The spectra acquired without the *trigger* function are used to confirm that the resonance of the isotropic peak is not affected by the phasing of the spectrum.

A set of rotor inserts was designed, intended to encapsulate the crystal inside the rotor and to hold it in a fixed position during the acquisition. A schematic of the insert is presented in Figure 2a. The insert consists of a plastic cylinder with a cavity in the middle that hosts the crystal. The cavity of each insert is designed to host a specific crystal aligned in a certain orientation. The insert is 3D-printed as two detached halves, which, once the crystal is aligned inside the cavity, are put together and the resulting cylinder is tightened in Teflon seal tape to ensure firmness inside the rotor. A photograph of half of the insert designed for Crystal 1 is shown in Figure 2b.

In the case of the static NMR acquisitions, the crystal under study was aligned in the 3D-printed insert along a certain crystallographic axis, and mounted inside the probe coil so that that specific axis was aligned parallel to the external field.

For each crystal, the NMR acquisition was repeated with alignment of each crystallographic axis a, b and c along either the rotor axis aligned at the magic angle (under MAS),

or the external magnetic field (under static conditions).

Calculation of the BMS Shift Tensor

Our approach to the calculation of the BMS shift implements a finite numerical model to calculate the internal demagnetizing field distribution within a crystal of a given shape, using the OOMMF code.[64] From Equation 3, the components of $\boldsymbol{N}(\boldsymbol{r})$ can be directly determined from the resulting $\boldsymbol{H_D}(\boldsymbol{r})$ when $\boldsymbol{M}$ points along each of the three principal crystal axes (e.g. $N_{ii}(\boldsymbol{r}) = H_{D,i}(\boldsymbol{r})/M_i$). To determine $\boldsymbol{N}(\boldsymbol{r})$, first the exact crystal shape is extracted from the analysis of high-resolution calibrated microscope images of the $LiFePO_4$ single crystals, and converted into a 3D mask. Where possible, individual face orientations and positions are determined to create the mask. For highly irregular and multifaceted samples (e.g. Crystal 3), where such an approach is infeasible, an outline mask is built up from images of the sample oriented along specific crystal planes (e.g. *ab*, *ac*, *bc* planes). The volume enclosed by this surface mask is then broken into a discrete mesh of approximately cuboid cells, with uniform (unit) magnetization, $\boldsymbol{M}$, throughout the crystal. The cell volume is adapted to simulate $\sim 10^6$ cells within each crystal to accurately map the crystal shape, and maintain the precision of the resulting field distribution. Within the numerical model, $\boldsymbol{M}$ is aligned in turn along the three principal axes of the crystal, and the volume average of $\boldsymbol{H}_D$ within each cell of the crystal is calculated, such that $\nabla \cdot \boldsymbol{B} = 0$. In the case of a perfect ellipsoid, the resulting vector field, $\boldsymbol{H}_D(\boldsymbol{r})$ is uniform. However, in the more complex geometries studied here $\boldsymbol{H}_D(\boldsymbol{r})$ is position-dependent, which ultimately provides a continuous distribution of BMS shifts experienced by the ^{7}Li nuclei. From the $\boldsymbol{H_D}(\boldsymbol{r})$ vector field (for a given direction of $\boldsymbol{M}$), and using Equation 3, $\boldsymbol{N}(\boldsymbol{r})$ is determined, which in this form is equivalent to the demagnetizing field per unit (induced) magnetization.

We now describe in detail the image masks, used to create numerical models of the investigated single crystals. For crystal 1, the relatively simple shape allowed precise facet planes to be identified. The indices for these planes, and separation from the designated

crystal origin, d are listed table S3 of the S.I. For the remaining samples, the crystal shapes are too complex to repeat this method. Instead images of the crystal oriented along the three principal crystallographic axes were taken, and an outline mask formed. Outline masks for crystals 2 and 3 in each of the three planes ab, ac and bc are shown in Figure 3(a). The 3D volume enclosed by these masks is fractured into a uniform grid of $\sim 10^6$ cells, each with unit induced magnetisation. A representative volume image of crystal 3, aligned along in the cb plane is shown in 3(b), along with the resulting magnetisation vector field map, $\boldsymbol{M}$, and numerically calculated demagnetising field, $\boldsymbol{H_D}$. Following Figure 3(b), the magnetisation of the volume is aligned along a specific crystallographic axis (in this case B_0, and so M, $\parallel$ c-axis), and the resulting demagnetising field is calculated, in order to maintain continuity of $\boldsymbol{B}$ across the crystal surface. From the resulting $\boldsymbol{H}$ vector field map, one can see the stray field external to the crystal, which in this case points predominantly in the $+c$ direction (red colour), and the internal (approximately uniform) demagnetising field, $\boldsymbol{H_D}$, which opposes $\boldsymbol{M}$ and is predominantly in the $-c$ direction (blue colour). Arrows represent subsampling of the vector field for clarity.

The $\boldsymbol{H_D}$ vector field within the crystal produces a position-dependent $\boldsymbol{N(r)}$ demagnetising tensor, and ultimately a range of shift values. The terms in this tensor are obtained by considering equation 3, in the limit that $\boldsymbol{M}$ lies along only one of the principal crystal axes. For the example shown, i.e. a crystal with unit magnetization parallel to the c-axis ($\boldsymbol{M} = (0, 0, 1)$), the discrete values of $H_{D,c}(r)$ throughout the crystal directly equate to the tensor component $N_{cc}(r)$. Using equation 4, therefore, by combining the array of $N_c c$ values with the experimental χ_c yields $\delta^{\mathrm{BMS}}_{\mathrm{calc.}}(\boldsymbol{B_0} \parallel \mathrm{c-axis})$. The total static shifts ($\boldsymbol{\delta}^{\mathrm{TOT}}_{\mathrm{calc.}} = \boldsymbol{\delta}^{\mathrm{BMS}}_{\mathrm{calc.}} + \boldsymbol{\delta}^{\mathrm{dip}}_{\mathrm{calc.}} + \delta^{s}_{\mathrm{local}} \cdot \mathbf{1}$) can then be obtained for the geometry in question. The range of $\delta^{\mathrm{TOT}}_{\mathrm{calc.}}$ for crystal 3, are shown as the green distribution in Figure S12 of the S.I.

Finally, to calculate the isotropic BMS shift under MAS, it is sufficient to take the average value of on-diagonal components of $\boldsymbol{N}(\boldsymbol{r})$ when calculating equation 5, since any dispersion in the values produces only line broadening in this case. The resulting average demagnetising

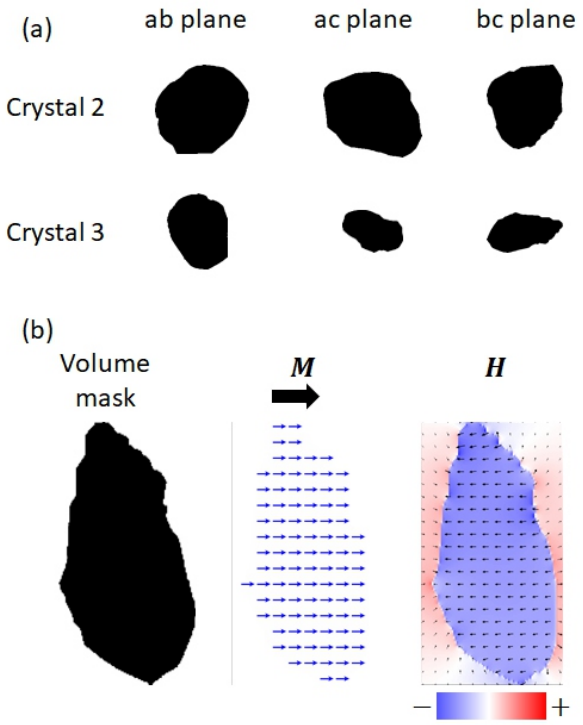

Figure 3: (a) Outline masks of crystals 2 and 3, shown along planes *ab*, *ac* and *bc*, built up from images taken of the crystals aligned along each of principal axes. The complex shape of these crystals make identifying individual facets infeasible. (b) Volume mask of crystal 3 aligned along the *bc* plane and the resulting demagnetising field distribution. The volume enclosed by this mask is fractured into cells, each containing unit magnetisation aligned along a chosen crystal axis. Micromagnetic simulations calculate the resulting demagnetising field, $\boldsymbol{H_D}(\boldsymbol{r})$, which can then be used to calculate $\boldsymbol{N}(\boldsymbol{r})$ throughout the crystal. The (uniform) magnetisation is aligned, in this case, along *c*-axis. Note, $\boldsymbol{H_D}(\boldsymbol{r})$ opposes $\boldsymbol{M}$ and is only slightly non-uniform for this case.

tensor, $\boldsymbol{N}^{\mathbf{iso}}$, for the three crystals under investigation are shown in Section S7 of the S.I., while $\delta^{\mathrm{BMS_{calc.}}}$ are shown in table 2 of the main article.

It now remains to calculate the resulting BMS shift. The numerically calculated $\boldsymbol{N}$ is combined with the experimentally measured $\boldsymbol{\chi}_{\mathrm{V}}$ of each crystal, using equation 4, to give $\boldsymbol{\delta}^{\mathrm{BMS}}$. This array of $\boldsymbol{\delta}^{\mathrm{BMS}}$ values is equivalent to the distribution of BMS shifts observed in static NMR experiments, and is compared to experimentally obtained patterns for $LiFePO_4$ in the S.I., along with a more detailed discussion of the applied numerical procedure. Once again, we note that these calculated shifts explicitly include any conventional BMS and ABMS effects. Finally, the volume average of the three on-diagonal components of $\boldsymbol{N}$ are obtained directly from this distribution and input into equation 5 to yield $\delta^{\mathrm{BMS_{calc.}}}$ for a given crystal.

$\delta^{\mathrm{BMS_{calc.}}}$ is then combined with the $\delta^{s}_{\mathrm{local}}$ to obtain the total shift, with $\delta^{s}_{\mathrm{local}}$ being taken from the experimental powder measurement. For completeness, the static ^{7}Li NMR pattern is simulated (as described in the S.I.) by combining $\boldsymbol{N}(\boldsymbol{r})$ with the full local shift tensor obtained from first principles DFT calculations by some of the present authors in a previous work[48] to give the full $\boldsymbol{\delta}^{s}$ tensor, and thus the full static pattern in the presence of the distribution of demagnetising fields.

Results and Discussion

Magnetic Susceptibility

Figure 4 shows the variation of the zero-field cooled molar magnetic susceptibility χ_i along each crystallographic axis i with temperature in the range of $2-301$ K for the three $LiFePO_4$ single crystals. The curves show that all the crystals are characterized by typical paramagnetic features over a wide temperature range and become antiferromagnetic at a Néel temperature (T_N) of 53 K. Below 52 K a substantial drop is observed in χ_b, while the change in both χ_a and χ_c is less prominent. This indicates the presence of antiferromagnetic long-

range order below T_N with the crystallographic b axis being the magnetic easy axis of the $LiFePO_4$ system. These results are in agreement with previously reported magnetic data on $LiFePO_4$ single crystals.[65]

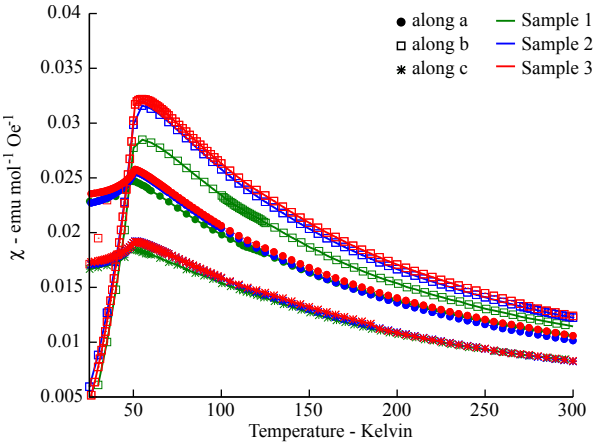

Figure 4: Experimental molar magnetic susceptibility curves of the three $LiFePO_4$ crystals as a function of temperature (green, blue and red for Crystal 1, 2 and 3, respectively). The measurement for each crystal mounted with the $a-$, $b-$ or $c-$ axis aligned with the field is represented with circle, square and star symbols, respectively.

For each susceptibility curve, the Weiss constant, θ, is extracted by fitting the Curie-Weiss law $\frac{1}{\chi} = \frac{T-\theta}{C}$, with C being the Curie constant, in the temperature range of $150-301$ K. The obtained Weiss constants are summarised in Table 1. The details of the fittings are presented in the S.I. (Figure S2 and Table S1). The trend $|\theta(\| b)| < |\theta(\| a)| < |\theta(\| c)|$ is obtained for all the crystals. The observed values and trend with respect to the alignment are in agreement with previously reported magnetic results.[65] From the fitting of the susceptibilities, shown in Figure S2 of the S.I., the value of χ at room temperature is extracted along each crystallographic axis (Table 1). This is then combined with $\boldsymbol{N}$ to calculate the demagnetising field, and hence the BMS shift, for each crystal.

Table 1: Dimensions (in mm), Weiss constants (in K) and χ values (in emu mol^{-1} Oe^{-1}) at 320 K of each $LiFePO_4$ crystal $1-3$ for the three a, b and c crystallographic axis.

	Dimensions mm			θ K			χ (320 K) emu mol^{-1} Oe^{-1}		
	a	b	c	a	b	c	a	b	c
Crystal 1	1.1	1.4	1.7	-127	-86	-135	0.0100	0.0109	0.0079
Crystal 2	1.7	1.9	2.1	-105	-89	-119	0.0097	0.0116	0.0079
Crystal 3	2.3	2.8	0.9	-112	-80	-121	0.0101	0.0118	0.0079

Powder Characterization with TEM, XRD and ^{7}Li MAS NMR Spectroscopy

The morphology of the crystallites and their average sizes in the $LiFePO_4$ powder were analysed with TEM. Two illustrative images are presented in Figure S3 of the S.I. A total of 30 particles were analysed. The particles show a featureless irregular morphology, with an average size distribution between 50 and 250 nm. Since the detection with TEM was made difficult by the carbon coating of the powder, the TEM results were compared with the analysis based on X-ray diffraction. The volume-weighted domain size, D_{V}, was determined by Rietveld refinement to be 100(3) nm. The fitting of the XRD pattern is shown in Figure S4 of the S.I. Under the assumption that the powder is a monodisperse system of spherical crystallites, this corresponds to an average crystallite diameter of 133(4) nm, and is within the range obtained by the direct particle measurement performed using TEM.

The ^{7}Li MAS NMR spectrum of the $LiFePO_4$ powder is shown in Figure 5, and an isotropic shift of $\delta^{\mathrm{iso}} = -16$ ppm is measured. Since we confirmed that the powder approximately corresponds to an ensemble of crystallites with featureless shapes, the isotropic shift of the $LiFePO_4$ powder is considered as resulting only from the local orbital, hyperfine and spin-orbit coupling interactions within the Ewald sphere, i.e. only $\boldsymbol{\delta}^s$ in equation 2.

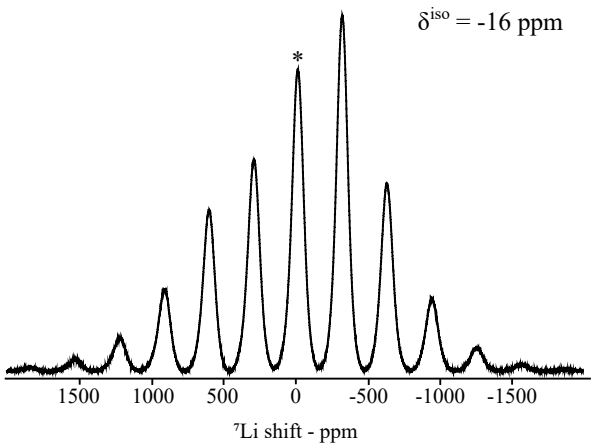

Figure 5: Experimental ^{7}Li solid-state NMR of the $LiFePO_4$ powder sample at 12.5 kHz MAS. The centreband is located at the isotropic shift of -16 ppm, and is marked with a $*$.

Single Crystal Solid-state ^{7}Li NMR Spectroscopy

The MAS NMR spectra of the three $LiFePO_4$ single crystals were acquired for each crystallographic axis aligned along the magic angle. The spectra obtained for the crystals with the *b*-axis aligned along the magic angle are shown in Figure 6. We see immediately that the spinning sidebands have different phases across the manifold, as expected for single-crystal NMR.[62] The spectra obtained for the alignment of the *a* and *c* axes along the rotor axis are shown in Figures S5 and S6 of the S.I. For each crystal, the variation of the isotropic shift between the different alignments is small, being within $\pm$ 3 ppm (Table S2 of the S.I.). The obtained shifts for each crystal are tabulated in Table 2 as the average of the values measured for the *a*, *b* and *c* alignments, ($\overline{\delta}_{\text{exp.}}$). In order to ensure that the values of the isotropic shifts did not depend on the phasing of the spectra, for every orientation the ^{7}Li NMR of the three samples was also acquired without applying the *trigger* in the NMR pulse sequence, as described in the Experimental Section. This resulted in spectra in which the spinning sidebands have the same phase. The ^{7}Li NMR spectra obtained with this approach are presented in the S.I. (Figure S7 to S9). No significant difference in the shift measured using the two NMR pulse sequences is observed.

As summarised in Table 2, a very large variation in $\overline{\delta}_{\text{exp.}}$ of almost 60 ppm is found

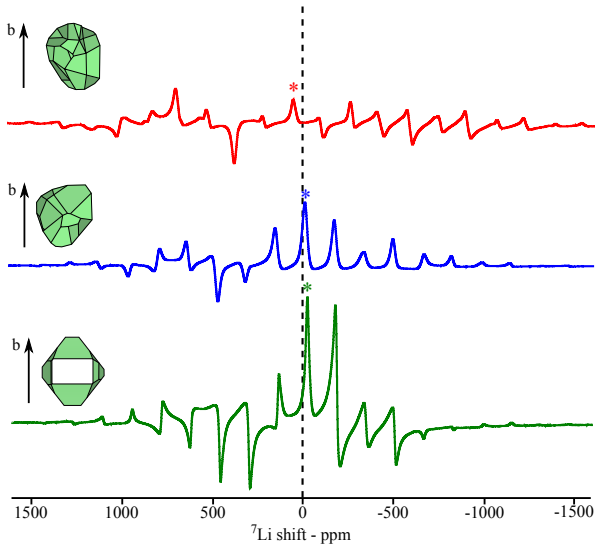

Figure 6: Experimental ^{7}Li NMR spectra of the three $LiFePO_4$ single crystals oriented with the b-axis aligned along the rotor axis inclined at the magic angle. Green, blue and red lines are used for Crystal 1, 2 and 3, respectively. The isotropic resonance is marked with a *.

Table 2: Comparison of the calculated and experimental isotropic shifts of ^{7}Li in the three $LiFePO_4$ crystals. The total calculated shift ($\delta^{\text{tot}}_{\text{calc.}}$) is computed using eq. 5, and is the sum of the bulk magnetic susceptibility contribution ($\delta^{\text{BMS}}_{\text{calc.}}$), and the local contribution (-16 ppm). The experimental isotropic ^{7}Li shift ($\overline{\delta}_{\text{exp.}}$) is the average of the shifts measured with each crystallographic axis a, b, and c aligned in turn along the rotor axis.

	$\delta^{\text{BMS}}_{\text{calc.}}$ ppm	$\delta^{\text{tot}}_{\text{calc.}}$ ppm	$\overline{\delta}_{\text{exp.}}$ ppm
Crystal 1	-5	-21	-21
Crystal 2	-1	-17	-20
Crystal 3	58	42	37

across the series, and the shift of each crystal deviates from the ^{7}Li shift of the powder sample (-16 ppm), with the latter assumed to correspond to the paramagnetic shift due to the local interactions within the Ewald sphere. Since the principal difference between the crystals is the shape, the large variation in their ^{7}Li NMR shifts is primarily ascribed to the bulk magnetic susceptibility effects. The calculated $\delta^{\text{BMS}}_{\text{calc.}}$ values are also presented in Table 2, and the results indeed support the hypothesis that the BMS shift varies significantly

between the crystals because of the different shapes and shape anisotropies of the three samples. The BMS shift is found to constitute a significant contribution to the total shift, in particular for Crystal 3. The total isotropic shifts are calculated as $\delta^{\text{tot}}_{\text{calc.}} = \delta^{\text{BMS}}_{\text{calc.}} + \delta^{s}_{\text{local}}$, where $\delta^{s}_{\text{local}} = -16$ ppm is the $LiFePO_4$ powder ^{7}Li shift (Table 2). The shifts calculated for the different crystals reproduce the experimental trend very well. The error in the BMS shift calculation for Crystal 3 is mainly ascribed to the approximations made to simulate the shape and size of the crystal. This crystal has a complex and multifaceted shape, making it difficult to model its morphology exactly. Furthermore, it is difficult to measure distances using the video microscope on the single crystal X-ray diffractometer precisely. Nevertheless, the calculations confirm that the model presented in this work is accurate, and the BMS shift can indeed be a significant contribution to the total shift. Depending on the magnetism and the macroscopic shape of the crystal, the BMS shift can be comparable to or of even greater size than the local Fermi-contact and pseudo-contact shifts.

Following the success of BMS modelling in accounting for the varying isotropic shifts under MAS measurement conditions, the study of the three $LiFePO_4$ crystals was extended to calculate the effect of the BMS on the whole shift tensor. The results are presented in the S.I. (Figures S10 to S12).

BMS Effects in Crystals of Arbitrary Shapes

To place our modelling results in a wider context within the field, particularly beyond single crystals, we now consider the analysis of the BMS shift in $LiFePO_4$ powders with varying particle shapes. Specifically, four $LiFePO_4$ powder crystallite morphologies will be now discussed, based on the previous computational work by Fisher and Islam,[66] as well as on previous experimental characterization studies.[12,13,67,68] For each crystallite, we calculated the ^{7}Li BMS shift contribution by simulating the reported particle morphology to obtain $\boldsymbol{N}$.[66] The magnetic susceptibility tensor used for these calculations was taken from the

results of the $LiFePO_4$ single crystals obtained in this work (Table 1). The values of the principal components of $\boldsymbol{\chi}$ that we used are averages over the three crystals: $\bar{\chi}_a$(Crystal 1, 2, 3), $\bar{\chi}_b$(Crystal 1, 2, 3), $\bar{\chi}_c$(Crystal 1, 2, 3). The total ^{7}Li NMR shift was calculated following the same procedure adopted throughout this work, whereby $\delta^{\mathrm{iso,TOT}}_{\mathrm{calc.}} = \delta^{\mathrm{BMS}}_{\mathrm{calc.}} + \delta^{s}_{\mathrm{local}}$, with $\delta^{s}_{\mathrm{local}} = -16$ ppm. Figure 7 shows the trend of the BMS shift in LiFePO for particles of all arbitrary shapes, plotted as a colour map. The results for the above-mentioned four particle shapes are also illustrated in the plot. The axes in Figure 7 represent the diagonal components of $\boldsymbol{N}$ along the a and b axes, N_a and N_b, as set by the particle's dimensions. The third component N_c is not shown for reasons of clarity, but is readily calculated from $N_c = 1 - (N_a + N_b)$. The corresponding plot showing all the three principal components is shown in Figure S14 of the S.I. To facilitate the interpretation of Figure 7, the demagnetising tensor calculated for each of the four particle morphologies is presented in Section S7 of the S.I.

This analysis allows us to identify a clear dependence of the sign and magnitude of the BMS shifts on the anisotropy in the crystallite shape. The more anisotropic plate-like (e.g. I and II) or needle-like $LiFePO_4$ particles show a greater absolute BMS shift contribution than the more isotropic block-like particles (e.g. III and IV). Furthermore, for the $LiFePO_4$ plate-like particles (I and II) where the b-axis – the magnetic easy axis – is along the shortest crystal dimension, and the (010) face is the one with the largest surface area, the BMS shift is predicted to be negative. By contrast, the $LiFePO_4$ block-like particles (III and IV), for which the b-axis is along the longest crystal dimension, and the (010) face is the smallest surface, are calculated to have a positive BMS shift. The results presented in Figure 7 are to be taken as approximate, due to the simplifications made when modelling the crystallite morphologies. Nevertheless, they represent a guideline to estimate the size and the sign of the BMS shift based on the shape of the $LiFePO_4$ particles. As a further consequence of the anisotropic $\boldsymbol{\chi}$ of $LiFePO_4$, the BMS shift is implicitly sensitive to the relative size of the crystallite (010) surface. Therefore, the sign and magnitude of the BMS shift can in

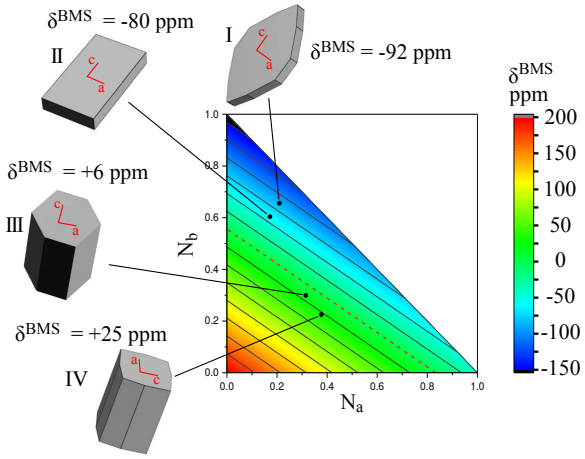

Figure 7: Analysis of the calculated BMS shift for $LiFePO_4$ powder crystallites. Four representative morphologies (labelled I to IV) are represented as schematics in grey. For each crystallite, the (a, c) crystallographic axes are indicated in red on the face normal to the b-axis. The corresponding bulk magnetic susceptibility ^{7}Li shift – δ(BMS) – and total isotropic ^{7}Li shift – δ(tot) – are also shown, calculated as in eq. 5. Also shown is the variation of the BMS shift as a function of the N_a (x-axis) and N_b (y-axis) principal components of the demagnetising tensor, $\boldsymbol{N}$. The variation with the third principal component N_c is not explicitly shown, but can be inferred from $N_c = 1 - (N_a + N_b)$. The colouring in the plot represents the δ(BMS) as determined by the relative (N_a vs N_b) morphology of the $LiFePO_4$ particle. The colouring scheme, indicated on the right-hand side, corresponds to the δ(BMS) range from -150 ppm (dark blue) to $+200$ ppm (red). The solid lines represent $+25$ ppm increments, and the dotted red line indicates 0 ppm. The points corresponding the BMS shifts of the four crystal morphologies are indicated on the plot.

principle constitute an indirect means to characterize the relative particle length along the [010] direction. This is particularly relevant for applications using $LiFePO_4$ as a cathode material in Li-ion batteries, because the [010] channel (normal to the (010) face) represents the easiest Li-ion conduction pathway, and control of its length during synthesis is often sought after.[12–14]

We also tested our approach against the ^{7}Li NMR results obtained by Hamelet *et al.* for a range of $LiFePO_4$ powders,[41] where both precise particle shape and isotropic shift have been obtained. In their work, two $LiFePO_4$ samples were prepared, with different particle morphologies. The corresponding SEM images and Rietveld refinement results are presented in Figure 1 and Table 1 of Ref. 41. These show that for one case (Sample A in Ref. 41),

the $LiFePO_4$ powder particles are micrometric featureless rounded crystallites. For the other case (Sample B in Ref. 41), the $LiFePO_4$ powder consists of nanometric plate-like particles. Hamelet *et al.* collected the ^{7}Li MAS NMR spectra of both samples, obtaining a ^{7}Li shift of -13 ppm for the featureless particles of Sample A, and -30 ppm for the anisotropic plate-like particles of Sample B. In order to see whether this difference in ^{7}Li shift between the two samples can be accounted for by changes in particle shape, we again applied our model by simulating the crystallites morphologies based on the information provided in Ref. 41. The rounded featureless particles of Sample A are not expected to show significant BMS effects, due to their approximately isotropic shape. Hence, following our approach, the total ^{7}Li shift is predicted to be dominated by the local contribution within the Ewald sphere, $\delta^s_{\text{local}} = -16$ ppm, in very close agreement to the experimental ^{7}Li shift of -13 ppm. For simplicity, the anisotropic plate-like particles of Sample B were simulated by considering ellipsoids with dimensions taken from the Rietveld refinement obtained by Hamelet *et al.* (30 nm along a, 32 nm along b and 47 nm along c).[41] This morphology is predicted by our model to give a BMS shift contribution of -32 ppm, hence a total ^{7}Li shift of -47 ppm. Qualitatively, our model appears to broadly reproduce the experimental result (-30 ppm), with both the approximate magnitude and negative sign of the overall ^{7}Li NMR shift accurately captured. In this case, referring to Figure 7 as guideline, the size and magnitude of the shift are due to both the anisotropic magnetic susceptibility, and the longer c axis dimension in Sample B, as compared with spherically symmetric Sample A. Quantitatively, a discrepancy of -17 ppm exists between simulation and experiment. However it is worth noting that, in this regime, any results are extremely sensitive to the exact dimensions used for the shape model. A modest ($\sim 10\%$) change in dimensions, for example, to (34 nm along a, 34 nm along b and 43 nm along c) predicts a BMS contribution of -15 ppm and a total shift of -30 ppm, closely matching the experimentally observed result.

This method of regressing particle shape to that of an ellipsoid, with equivalent major and minor axes, represents a significant simplification to numerically modelling the exact

crystal, with two notable advantages. First, as the demagnetising field is uniform within an ellipse, off-diagonal terms in N are zero. Second, analytical solutions exist to calculate the remaining three on-diagonal components, providing an easily employable means to estimate δ^{BMS}. Since such simplicity offers a practical approach for others to considering BMS effects, we discuss the applicability of this ellipse regression more broadly, noting initially that the comparison with the results of Hamelet *et al.* indicate at least qualitative agreement is readily achievable. As an illustrative case, we applied the approach to single crystals 1, 2 and 3 discussed earlier. In this test the ellipsoid axes were set as the extreme dimensions of each crystal, giving δ^{BMS} = -21, -24 and +25 ppm for crystals 1, 2 and 3, respectively. Clearly, the method accurately reflects the sign of the BMS shifts and magnitude in each case, but lacks the overall quantitative agreement of the full calculations. It is illuminating that crystal 3, the most irregular shaped sample, should provide the poorest quantitative agreement in this case. This highlights a general challenge with applying such a simplifying method. The BMS effect is highly sensitive to the precise crystal shape and so application of such a method requires accurate regression, a particular problem when considering highly irregular-shaped crystals. We imagine using a numerical procedure to determine a bestfit ellipse, rather than simply taking the extreme dimensions, would more accurately regress the crystal, and so provide better estimates of BMS, but such methods are beyond the scope here. Neverthless, as an estimate of both the sign and magnitude of the effect, ellipse regression offers a practical means to gauge the BMS contribution. We note for powder samples, averaging across the random variations between crystallites will likely converge towards a regular-shaped mean crystallite. Now the average dimensions, e.g. determined via XRD, should accurately reflect this uniform average shape. We anticipate, therefore, that the process of determining N from an equivalent ellipse to be quite accurate in this case, and should provide a useful means to quantitatively estimate BMS shift from powder shape analysis.

Finally, it is worth highlighting the potential applications for the reverse approach. As

noted earlier, the BMS shift is highly sensitive to crystal dimensions. Conversely, given δ^{BMS}, and with knowledge of χ, it is possible to back calculate N, and so shape. Unfortunately, δ^{BMS} does not uniquely map to a set of N_{xx} N_{yy} N_{zz}, however, in most cases the constraints $Tr(N) = 1$ and Eq. 4 are sufficient to define the extreme crystal axes. Indeed, if the approximate shape is known, e.g. an ellipsoid of revolution, aspect ratio can be precisely determined via the BMS shift. Earlier, we indicated the importance of this observation in assessing crystal length in the [010] direction for $LiFePO_4$ (a key conduction pathway for the battery material), where positive shifts were shown to indicate a long axis in the [010], compared with a short axis for negative shifts. More broadly, for any NMR study into materials where crystal shape directly impacts the macroscopic properties of interest, these results demonstrate a means to use the isotropic ABMS shift as a probe of morphology, potentially avoiding the need for separate characterisation via TEM or XRD.

Implications for other systems

The significant contribution of the ABMS effects to the total NMR shift is not a unique characteristic of $LiFePO_4$, but it can be expected for any system with large and anisotropic susceptibility, and non-spherical particle shape. The anisotropy of the magnetic susceptibility arises from the spin-orbit coupling interaction at the paramagnetic centres in the system. To illustrate with systems that are isostructural to $LiFePO_4$, olivine-type $LiCoPO_4$ and $LiNiPO_4$ are reported to have an anisotropy of the spin-orbit coupling interaction even greater than that of $LiFePO_4$, due to the *d*-orbital configuration of the high-spin Co^{2+} and Ni^{2+} ions.[48,69–72] Consequently, for particles of anisotropic shapes, even greater ABMS shift contributions are expected to the ^{7}Li NMR spectra of $LiCoPO_4$ and $LiNiPO_4$. To broaden the examples beyond the olivine-type systems just discussed, Ni and Co ions are also often found in the layered Li-rich Mn-based oxides, lithium nickel manganese cobaltates (NMC) and Al-substituted lithium nickel cobaltates, all of significant practical interest as cathode materials in rechargeable Li-ion batteries. As an example, the electrochemical properties

of $Li_{1.2}Co_{0.13}Ni_{0.13}Mn_{0.54}O_2$ have been studied in relation to different particle morphology, and superior performances of oblong olive-like morphology have been reported.[73] Commercial NMC and NCA particles generally consist of large (approximately 10) micron sized spherical particles formed by fused rod/platelet-like primary particles. Significant particle cracking occurs on battery cycling.[74]

Determining how the anisotropic particle shapes of the primary particles and their susceptibilities at different states of charge, affect the ABMS shifts, may yield increased insight into the solid-state ^{7}Li NMR spectra of these samples. Furthermore, the present model can be extended to incorporate the effect of preferred orientation of non-spherical particles in powders. Here, even for systems (or states of charge in a battery sample) with isotropic magnetic susceptibility, non-zero shift contributions are expected to arise, which will not be removed under MAS.

Spin-orbit coupling effects are typically even stronger for heavier metals of spin quantum number $S > \frac{1}{2}$ such as lanthanides.[75] Hence, considerable ABMS shifts are likely to arise for particles of non-cubic symmetry containing lanthanide ions.

ABMS shifts are not exclusive to paramagnetic systems, but are relevant also in the case of diamagnetic materials. One important example to this regard is graphite, for which the relative magnetic susceptibility varies by two orders of magnitude between the directions parallel and perpendicular to the aromatic planes.[76] Because of such a large susceptibility anisotropy, depending on the shape of the graphite particles, and on the orientation of the susceptibility tensor within the particles, ABMS effects should lead to considerable contributions to the ^{13}C isotropic shift.

Conclusions

This work shows that the NMR shift of a paramagnetic material with anisotropic susceptibility does not only depend on the local environment of the observed nucleus, but it is also a function of the shape of the particles under investigation. Starting from an approach commonly used in the physics community to calculate demagnetising fields in magnetic structures, we present a method to link the morphology of a paramagnetic crystal/particle and the bulk magnetic susceptibility of the material to the measured NMR shift. We apply the model to the analysis of the ^{7}Li NMR spectra of $LiFePO_4$, providing answers to a long-lasting question in the literature as to why different $LiFePO_4$ samples are found to have very different ^{7}Li NMR shifts. We first test the model on a set of $LiFePO_4$ single crystals of different shapes. We find that the measured ^{7}Li shifts of the different $LiFePO_4$ crystals vary significantly, covering a range of almost 60 ppm. Our simulations, based on the local hyperfine contribution to the shift, and the macroscopic contribution due to the $LiFePO_4$ bulk magnetic susceptibility and the shape of each crystal, confirm that the large ^{7}Li NMR shift variation between the samples is due to the different morphologies of the crystals, giving rise to very different BMS shift contributions. We then extend the study to the analysis of $LiFePO_4$ powders, confirming the direct dependece of the sign and magnitude of the ^{7}Li NMR shift to the anisotropy of the particles aspect ratio, with platelet shaped particles giving rise to BMS shift close to -80 ppm, rod shaped particles resulting in BMS shifts greater than 5 ppm. Based on our results, we present an approach to estimate the size and the sign of the NMR shift based on the morphology of the $LiFePO_4$ particles, which can alternatively be used as a method to infer the particle shape based on the measured ^{7}Li NMR shift. The approach can be extended to the analysis of other systems with significant magnetic anisotropy, such as other electrode materials used in energy storage devices. Of note, these are systems for which many of their electrochemical properties depend indeed on the particle shape and size.

Acknowledgements

The authors would like to thank Fiona Strobridge for the synthesis of the $LiFePO_4$ powder. Dr. Siân Dutton, Dr. Hajime Shinohara and Dr. Paromita Mukherjee are also thanked for useful discussion and for the help with the SQUID measurements, and George Lane for the help with the 3D-printing. The authors are thankful to Dr. Ieuan Seymour, Dr. David Halat and Jeongjae Lee for useful discussions. R.P. acknowledges financial support from the People Programme (Marie Curie Actions) of the European Union's Seventh Framework Programme (FP7/2007-2013) under REA Grant Agreement no. 317127. R.P. and A.J.P. acknowledge funding from the Assistant Secretary for Energy Efficiency and Renewable Energy, Office of Vehicle Technologies, of the U.S. DOE under Contract no. DE-AC02-05CH11231, under the Batteries for Advanced Transportation Technologies (BATT) Program subcontract no. 7057154. MWG is grateful for support from the European Union's Horizon 2020 research and innovation programme under the Marie Skodowska-Curie grant agreement No. 659764. This work was carried out with the support of the Diamond Light Source (proposal EE13911).

Supporting Information

Demagnetising tensor for ideal morphologies, SQUID results for $LiFePO_4$, TEM and XRD of $LiFePO_4$ powder sample, static and MAS ^{7}Li NMR of $LiFePO_4$ single crystals, dipolar hyperfine tensor and BMS shift calculation details.

References

(1) Pell, A. J.; Pintacuda, G.; Grey, C. P. *Paramagnetic NMR in solution and the solid state*; Elsevier, 2018.

(2) Blanc, F.; Copéret, C.; Lesage, A.; Emsley, L. High resolution solid state NMR spectroscopy in surface organometallic chemistry: access to molecular understanding of

active sites of well-defined heterogeneous catalysts. *Chemical Society Reviews* **2008**, *37*, 518–526.

(3) Bertini, I.; Luchinat, C.; Parigi, G.; Pierattelli, R. Perspectives in paramagnetic NMR of metalloproteins. *Dalton Transactions* **2008**, 3782–3790.

(4) Knight, M. J.; Pell, A. J.; Bertini, I.; Felli, I. C.; Gonnelli, L.; Pierattelli, R.; Herrmann, T.; Emsley, L.; Pintacuda, G. Structure and backbone dynamics of a microcrystalline metalloprotein by solid-state NMR. *Proceedings of the National Academy of Sciences* **2012**, *109*, 11095–11100.

(5) Clément, R. J.; Middlemiss, D. S.; Seymour, I. D.; Ilott, A. J.; Grey, C. P. Insights into the Nature and Evolution upon Electrochemical Cycling of Planar Defects in the β-NaMnO2 Na-Ion Battery Cathode: An NMR and First-Principles Density Functional Theory Approach. *Chemistry of Materials* **2016**, *28*, 8228–8239.

(6) Seymour, I. D.; Middlemiss, D. S.; Halat, D. M.; Trease, N. M.; Pell, A. J.; Grey, C. P. Characterizing oxygen local environments in paramagnetic battery materials via ^{17}O NMR and DFT calculations. *Journal of the American Chemical Society* **2016**, *138*, 9405–9408.

(7) Carlier, D.; Ménétrier, M.; Grey, C. P.; Delmas, C.; Ceder, G. Understanding the NMR shifts in paramagnetic transition metal oxides using density functional theory calculations. *Physcal Review B* **2003**, *67*, 174103.

(8) Zhou, L.; Leskes, M.; Ilott, A. J.; Trease, N. M.; Grey, C. P. Paramagnetic electrodes and bulk magnetic susceptibility effects in the in situ NMR studies of batteries: Application to $Li_{1.08}Mn_{1.92}O_4$ spinels. *Journal of Magnetic Resonance* **2013**, *234*, 44–57.

(9) Trease, N. M.; Zhou, L.; Chang, H. J.; Zhu, B. Y.; Grey, C. P. In situ NMR of lithium ion batteries: Bulk susceptibility effects and practical considerations. *Solid state nuclear magnetic resonance* **2012**, *42*, 62–70.

(10) Grey, C. P.; ; Dupré, N. NMR Studies of Cathode Materials for Lithium-Ion Rechargeable Batteries. *Chemical Reviews* **2004**, *104*, 4493–4512.

(11) Pecher, O.; Carretero-González, J.; Griffith, K. J.; Grey, C. P. Materials methods: NMR in battery research. *Chem. Mater* **2017**, *29*, 213–242.

(12) Franger, S.; Le Cras, F.; Bourbon, C.; Rouault, H. Comparison between different $LiFePO_4$ synthesis routes and their influence on its physico-chemical properties. *Journal of Power Sources* **2003**, *119*, 252–257.

(13) Franger, S.; Le Cras, F.; Bourbon, C.; Benoit, C.; Soudan, P.; Santos-Peña, J. Overview on the practical electrochemical behaviour of optimized lithium iron phosphate. *Recent Res. Dev. Electrochem* **2005**, *8*, 225.

(14) Kim, D.-H.; Kim, J. Synthesis of $LiFePO_4$ nanoparticles in polyol medium and their electrochemical properties. *Electrochemical and Solid-State Letters* **2006**, *9*, A439–A442.

(15) Clauss, J.; Schmidt-Rohr, K.; Spiess, H. W. Determination of domain sizes in heterogeneous polymers by solid-state NMR. *Acta Polymerica* **1993**, *44*, 1–17.

(16) Tracht, U.; Wilhelm, M.; Heuer, A.; Feng, H.; Schmidt-Rohr, K.; Spiess, H. W. Length scale of dynamic heterogeneities at the glass transition determined by multidimensional nuclear magnetic resonance. *Physical Review Letters* **1998**, *81*, 2727.

(17) Schlagnitweit, J.; Tang, M.; Baias, M.; Richardson, S.; Schantz, S.; Emsley, L. A solid-state NMR method to determine domain sizes in multi-component polymer formulations. *Journal of Magnetic Resonance* **2015**, *261*, 43–48.

(18) Schlagnitweit, J.; Tang, M.; Baias, M.; Richardson, S.; Schantz, S.; Emsley, L. Nanostructure of materials determined by relayed paramagnetic relaxation enhancement. *Journal of the American Chemical Society* **2015**, *137*, 12482–12485.

(19) Pinon, A. C.; Schlagnitweit, J.; Berruyer, P.; Rossini, A. J.; Lelli, M.; Socie, E.; Tang, M.; Pham, T.; Lesage, A.; Schantz, S. Measuring nano-to microstructures from relayed dynamic nuclear polarization NMR. *The Journal of Physical Chemistry C* **2017**, *121*, 15993–16005.

(20) Spiess, H. W. 50th Anniversary perspective: the importance of NMR spectroscopy to macromolecular Science. *Macromolecules* **2017**, *50*, 1761–1777.

(21) McConnell, H. M.; Chesnut, D. B. Theory of Isotropic Hyperfine Interactions in π-Electron Radicals. *The Journal of Chemical Physics* **1958**, *28*, 107–117.

(22) McConnell, H. M.; Robertson, R. E. Isotropic nuclear resonance shifts. *The Journal of Chemical Physics* **1958**, *29*, 1361–1365.

(23) Kurland, R. J.; McGarvey, B. R. Isotropic NMR shifts in transition metal complexes: the calculation of the Fermi contact and pseudocontact terms. *Journal of Magnetic Resonance (1969)* **1970**, *2*, 286–301.

(24) Kaupp, M.; Köhler, F. H. Combining NMR spectroscopy and quantum chemistry as tools to quantify spin density distributions in molecular magnetic compounds. *Coordination Chemistry Reviews* **2009**, *253*, 2376–2386.

(25) Pennanen, T. O.; Vaara, J. Nuclear magnetic resonance chemical shift in an arbitrary electronic spin state. *Physical review letters* **2008**, *100*, 133002.

(26) Van den Heuvel, W.; Soncini, A. NMR Chemical Shift in an Electronic State with Arbitrary Degeneracy. *Physical review letters* **2012**, *109*, 073001.

(27) Schwerk, U.; Michel, D.; Pruski, M. Local magnetic field distribution in a polycrystalline sample exposed to a strong magnetic field. *Journal of Magnetic Resonance, Series A* **1996**, *119*, 157–164.

(28) Kubo, A.; Spaniol, T. P.; Terao, T. The effect of bulk magnetic susceptibility on solid state NMR spectra of paramagnetic compounds. *Journal of Magnetic Resonance* **1998**, *133*, 330–340.

(29) Drain, L. The broadening of magnetic resonance lines due to field inhomogeneities in powdered samples. *Proceedings of the Physical Society* **1962**, *80*, 1380.

(30) VanderHart, D.; Earl, W. L.; Garroway, A. Resolution in ^{13}C NMR of organic solids using high-power proton decoupling and magic-angle sample spinning. *Journal of Magnetic Resonance (1969)* **1981**, *44*, 361–401.

(31) Alla, M.; Lippmaa, E. Resolution limits in magic-angle rotation NMR spectra of polycrystalline solids. *Chemical Physics Letters* **1982**, *87*, 30–33.

(32) O'Handley, R. C. *Modern magnetic materials: principles and applications*; Wiley, 2000.

(33) Grey, C. P.; Dobson, C. M.; Cheetham, A. K. Susceptibility matching in MAS NMR. The determination of hyperfine tensors from paramagnetic stannates. *Journal of Magnetic Resonance (1969)* **1992**, *98*, 414–420.

(34) Dickinson, R.; Royappa, A. T.; Tone, F.; Ujj, L.; Wu, G. Distribution of non-uniform demagnetization fields in paramagnetic bulk solids. *Journal of Applied Physics* **2011**, *110*, 013902.

(35) Padhi, A. K.; Nanjundaswamy, K. S.; Goodenough, J. B. Phospho-olivines as positive-electrode materials for rechargeable lithium batteries. *Journal of the electrochemical society* **1997**, *144*, 1188–1194.

(36) Kabalov, Y.; Simonov, M.; Ivanov, V.; Melnikov, O.; Belov, N. Crystalline structure of Li(Fe,Zn)[PO_4]. *Doklady Akademii Nauk SSSR* **1973**, *208*, 1346–1348.

(37) Rousse, G.; Rodriguez-Carvajal, J.; Patoux, S.; Masquelier, C. Magnetic structures of

the triphylite $LiFePO_4$ and of its delithiated form FePO4. *Chemistry of materials* **2003**, *15*, 4082–4090.

(38) Tucker, M. C.; Doeff, M. M.; Richardson, T. J.; Finones, R.; Reimer, J. A.; Cairns, E. J. ^7Li and ^{31}P magic angle spinning nuclear magnetic resonance of $LiFePO_4$-type materials. *Electrochemical and solid-state letters* **2002**, *5*, A95–A98.

(39) Tucker, M. C.; Doeff, M. M.; Richardson, T. J.; Finones, R.; Cairns, E. J.; Reimer, J. A. Hyperfine fields at the Li site in $LiFePO_4$-type olivine materials for lithium rechargeable batteries: a ^7Li MAS NMR and SQUID study. *Journal of the American Chemical Society* **2002**, *124*, 3832–3833.

(40) Wilcke, S.; Lee, Y.-J.; Cairns, E.; Reimer, J. Covalency measurements via NMR in Lithium Metal Phosphates. *Applied Magnetic Resonance* **2007**, *32*, 547–563.

(41) Hamelet, S.; Gibot, P.; Casas-Cabanas, M.; Bonnin, D.; Grey, C. P.; Cabana, J.; Leriche, J.-B.; Rodriguez-Carvajal, J.; Courty, M.; Levasseur, S. The effects of moderate thermal treatments under air on $LiFePO_4$-based nano powders. *Journal of Materials Chemistry* **2009**, *19*, 3979–3991.

(42) Cabana, J.; Shirakawa, J.; Chen, G.; Richardson, T. J.; Grey, C. P. MAS NMR study of the metastable solid solutions found in the $LiFePO_4$/FePO4 system. *Chemistry of Materials* **2010**, *22*, 1249–1262.

(43) Clément, R. J.; Pell, A. J.; Middlemiss, D. S.; Strobridge, F. C.; Miller, J. K.; Whittingham, M. S.; Emsley, L.; Grey, C. P.; Pintacuda, G. Spin-transfer pathways in paramagnetic lithium transition-metal phosphates from combined broadband isotropic solid-state MAS NMR spectroscopy and DFT calculations. *Journal of the American Chemical Society* **2012**, *134*, 17178–17185.

(44) Bertini, I.; Luchinat, C.; Parigi, G. Magnetic susceptibility in paramagnetic NMR. *Progress in Nuclear Magnetic Resonance Spectroscopy* **2002**, *40*, 249–273.

(45) Hrobárik, P.; Reviakine, R.; Arbuznikov, A. V.; Malkina, O. L.; Malkin, V. G.; Köhler, F. H.; Kaupp, M. Density functional calculations of NMR shielding tensors for paramagnetic systems with arbitrary spin multiplicity: Validation on 3 d metallocenes. *The Journal of chemical physics* **2007**, *126*, 024107.

(46) Liimatainen, H.; Pennanen, T. O.; Vaara, J. 1H chemical shifts in nonaxial, paramagnetic chromium (III) complexesApplication of novel pNMR shift theory. *Canadian Journal of Chemistry* **2009**, *87*, 954–964.

(47) Lee, J.; Seymour, I. D.; Pell, A. J.; Dutton, S. E.; Grey, C. P. A systematic study of ^{25}Mg NMR in paramagnetic transition metal oxides: applications to Mg-ion battery materials. *Physical Chemistry Chemical Physics* **2017**, *19*, 613–625.

(48) Pigliapochi, R.; Pell, A. J.; Seymour, I. D.; Ceresoli, D.; Kaupp, M.; Grey, C. P. DFT investigation of the effect of spin-orbit coupling on the NMR shifts in paramagnetic solids. *Physical Review B* **2017**, *95*, 054412.

(49) Mondal, A.; Kaupp, M. Quantum-Chemical Approach to NMR Chemical Shifts in Paramagnetic Solids Applied to $LiFePO_4$ and $LiCoPO_4$. *The Journal of Physical Chemistry Letters* **2018**, *9*, 1480–1484.

(50) Blundell, S. *Magnetism in Condensed Matter Oxford Master Series in Condensed Matter Physics*; Oxford University Press USA, 2001.

(51) Dickinson, W. C. The Time Average Magnetic Field at the Nucleus in Nuclear Magnetic Resonance Experiments. *Physical Review* **1982**, *81*, 717.

(52) Garroway, A. N. Magic-Angle Sample Spinning of Liquids. *Journal of Magnetic Resonance* **1951**, *49*, 168.

(53) Janssen, Y.; Santhanagopalan, D.; Qian, D.; Chi, M.; Wang, X.; Hoffmann, C.;

Meng, Y. S.; Khalifah, P. G. Reciprocal salt flux growth of $LiFePO_4$ single crystals with controlled defect concentrations. *Chemistry of Materials* **2013**, *25*, 4574–4584.

(54) Strobridge, F. C.; Middlemiss, D. S.; Pell, A. J.; Leskes, M.; Clément, R. J.; Pourpoint, F.; Lu, Z.; Hanna, J. V.; Pintacuda, G.; Emsley, L. Characterising local environments in high energy density Li-ion battery cathodes: a combined NMR and first principles study of $LiFe_xCo_{1-x}PO_4$. *Journal of Materials Chemistry A* **2014**, *2*, 11948–11957.

(55) Coelho, A. A. TOPAS V2.0: General Profile and Structure Analysis Software for Powder Diffraction Data. *Bruker AXS: Karlsruhe, Germany* **2000**,

(56) Nytén, A.; Thomas, J. O. A neutron powder diffraction study of $LiCo_xFe_{1-x}PO_4$ for x= 0, 0.25, 0.40, 0.60 and 0.75. *Solid State Ionics* **2006**, *177*, 1327–1330.

(57) Balzar, D.; Audebrand, N.; Daymond, M.; Fitch, A.; Hewat, A.; Langford, J.; Le Bail, A.; Louër, D.; Masson, O.; McCowan, C. N. Size–strain line-broadening analysis of the ceria round-robin sample. *Journal of Applied Crystallography* **2004**, *37*, 911–924.

(58) Balzar, D. Voigt-function model in diffraction line-broadening analysis. *International union of crystallography monographs on crystallography* **1999**, *10*, 94–126.

(59) Pell, A. J.; Pintacuda, G. Broadband solid-state MAS NMR of paramagnetic systems. *Progress in nuclear magnetic resonance spectroscopy* **2015**, *84-85*, 33–72.

(60) Kervern, G.; Pintacuda, G.; Emsley, L. Fast adiabatic pulses for solid-state NMR of paramagnetic systems. *Chemical physics letters* **2007**, *435*, 157–162.

(61) Hwang, T.-L.; van Zijl, P. C.; Garwood, M. Fast broadband inversion by adiabatic pulses. *Journal of Magnetic Resonance* **1998**, *133*, 200–203.

(62) Levitt, M. H. Why do spinning sidebands have the same phase? *Journal of Magnetic Resonance (1969)* **1989**, *82*, 427–433.

(63) Pell, A. J.; Clément, R. J.; Grey, C. P.; Emsley, L.; Pintacuda, G. Frequency-stepped acquisition in nuclear magnetic resonance spectroscopy under magic angle spinning. *The Journal of chemical physics* **2013**, *138*, 114201.

(64) Donahue, M. J.; Porter, D. G. *OOMMF User's Guide, Version 1.0*; National Institute of Standards and Technology, Gaithersburg, MD, 1999; Vol. Interagency Report NISTIR 6376.

(65) Chen, D.; Wang, X.; Hu, Y.; Lin, C.; Dou, S.; Nigam, R. Magnetic anisotropy in doped and undoped $LiFePO_4$ single crystals. *Journal of applied physics* **2007**, *101*, 09N512.

(66) Fisher, C. A.; Islam, M. S. Surface structures and crystal morphologies of $LiFePO_4$: relevance to electrochemical behaviour. *Journal of Materials Chemistry* **2008**, *18*, 1209–1215.

(67) Ellis, B.; Kan, W. H.; Makahnouk, W.; Nazar, L. Synthesis of nanocrystals and morphology control of hydrothermally prepared $LiFePO_4$. *Journal of Materials Chemistry* **2007**, *17*, 3248–3254.

(68) Chen, G.; Song, X.; Richardson, T. J. Electron microscopy study of the $LiFePO_4$ to FePO4 phase transition. *Electrochemical and Solid-State Letters* **2006**, *9*, A295–A298.

(69) Singh, V.; Gershinsky, Y.; Kosa, M.; Dixit, M.; Zitoun, D.; Major, D. T. Magnetism in olivine-type $LiCo_{1-x}Fe_xPO_4$ cathode materials: bridging theory and experiment. *Physical Chemistry Chemical Physics* **2015**, *17*, 31202–31215.

(70) Vaknin, D.; Zarestky, J.; Miller, L.; Rivera, J.-P.; Schmid, H. Weakly coupled antiferromagnetic planes in single-crystal $LiCoPO_4$. *Physical Review B* **2002**, *65*, 224414.

(71) Baek, S.-H.; Klingeler, R.; Neef, C.; Koo, C.; Büchner, B.; Grafe, H.-J. Unusual spin fluctuations and magnetic frustration in olivine and non-olivine $LiCoPO_4$ detected by ^{31}P and ^{7}Li nuclear magnetic resonance. *Physical Review B* **2014**, *89*, 134424.

(72) Goni, A.; Lezama, L.; Barberis, G.; Pizarro, J.; Arriortua, M.; Rojo, T. Magnetic properties of the $LiMPO_4$ (M= Co, Ni) compounds. *Journal of magnetism and magnetic materials* **1996**, *164*, 251–255.

(73) Wang, G.; Yi, L.; Yu, R.; Wang, X.; Wang, Y.; Liu, Z.; Wu, B.; Liu, M.; Zhang, X.; Yang, X. $Li_{1.2}Ni_{0.13}Co_{0.13}Mn_{0.54}O_2$ with controllable morphology and size for high performance lithium-ion batteries. *ACS applied materials & interfaces* **2017**, *9*, 25358–25368.

(74) Tsai, P.-C.; Wen, B.; Wolfman, M.; Choe, M.-J.; Pan, M. S.; Su, L.; Thornton, K.; Cabana, J.; Chiang, Y.-M. Single-particle measurements of electrochemical kinetics in NMC and NCA cathodes for Li-ion batteries. *Energy & Environmental Science* **2018**, *11*, 860–871.

(75) Bleaney, B. Nuclear magnetic resonance shifts in solution due to lanthanide ions. *Journal of Magnetic Resonance (1969)* **1972**, *8*, 91–100.

(76) Goze-Bac, C.; Latil, S.; Lauginie, P.; Jourdain, V.; Conard, J.; Duclaux, L.; Rubio, A.; Bernier, P. Magnetic interactions in carbon nanostructures. *Carbon* **2002**, *40*, 1825–1842.

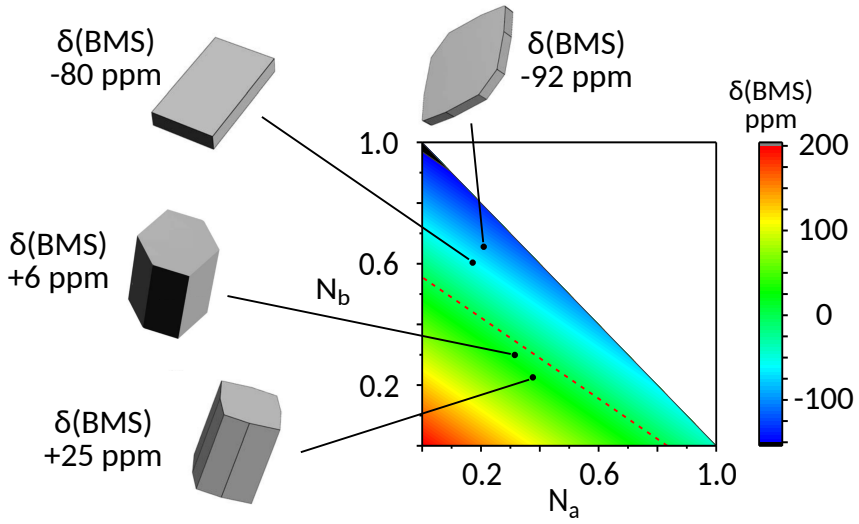
δ(BMS)
-80 ppm
δ(BMS)
-92 ppm
δ(BMS)
+6 ppm
δ(BMS)
+25 ppm
δ(BMS)
ppm
200
100
0
-100
1.0
0.6
0.2
N_b
0.2
0.6
1.0
N_a